REPORT DOCUMENTATION PAGE

Form Approved OMB NO. 0704-0188

1. REPORT DATE (DD-MM-YYYY)	2. REPORT TYPE	3. DATES COVERED (From - To)
	New Reprint	-

4. TITLE AND SUBTITLE	5a. CONTRACT NUMBER
Ballistic-Failure Mechanisms in Gas Metal Arc Welds of Mil A46100 Armor-Grade Steel: A Computational Investigation	W911NF-11-1-0207
	5b. GRANT NUMBER
	5c. PROGRAM ELEMENT NUMBER
	622105

6. AUTHORS	5d. PROJECT NUMBER
M. Grujicic, J. S. Snipes, R. Galgalikar, S. Ramaswami, R. Yavari, C.-F. Yen, B. A. Cheeseman	
	5e. TASK NUMBER
	5f. WORK UNIT NUMBER

7. PERFORMING ORGANIZATION NAMES AND ADDRESSES	8. PERFORMING ORGANIZATION REPORT NUMBER
Clemson University 300 Brackett Hall Box 345702 Clemson, SC 29634 -5702	

9. SPONSORING/MONITORING AGENCY NAME(S) AND ADDRESS (ES)	10. SPONSOR/MONITOR'S ACRONYM(S)
U.S. Army Research Office P.O. Box 12211 Research Triangle Park, NC 27709-2211	ARO
	11. SPONSOR/MONITOR'S REPORT NUMBER(S)
	57228-EG.30

12. DISTRIBUTION AVAILIBILITY STATEMENT
Approved for public release; distribution is unlimited.

13. SUPPLEMENTARY NOTES
The views, opinions and/or findings contained in this report are those of the author(s) and should not contrued as an official Department of the Army position, policy or decision, unless so designated by other documentation.

14. ABSTRACT

In our recent work, a multi-physics computational model for the conventional Gas Metal Arc Welding (GMAW) joining process was introduced. The model is of a modular type and comprises five modules, each designed to handle a specific aspect of the GMAW process, i.e.: (i) electro-dynamics of the welding-gun; (ii) radiation-/convection-controlled heat transfer from the electric arc to the workpiece and mass transfer from the filler-metal consumable electrode to the weld; (iii) prediction of the temporal evolution and the spatial distribution of thermal and mechanical fields within the weld region during the GMAW joining process; (iv) the resulting temporal

15. SUBJECT TERMS
Gas Metal Arc Welding (GMAW) Process Modeling; Ballistic Limit; Welded All-metal Armor

16. SECURITY CLASSIFICATION OF:			17. LIMITATION OF ABSTRACT	15. NUMBER OF PAGES	19a. NAME OF RESPONSIBLE PERSON
a. REPORT	b. ABSTRACT	c. THIS PAGE	UU		Mica Grujicic
UU	UU	UU			19b. TELEPHONE NUMBER
					864-656-5639

Report Title

Ballistic-Failure Mechanisms in Gas Metal Arc Welds of Mil A46100 Armor-Grade Steel: A Computational Investigation

ABSTRACT

In our recent work, a multi-physics computational model for the conventional Gas Metal Arc Welding (GMAW) joining process was introduced. The model is of a modular type and comprises five modules, each designed to handle a specific aspect of the GMAW process, i.e.: (i) electro-dynamics of the welding-gun; (ii) radiation-/convection-controlled heat transfer from the electric arc to the workpiece and mass transfer from the filler-metal consumable electrode to the weld; (iii) prediction of the temporal evolution and the spatial distribution of thermal and mechanical fields within the weld region during the GMAW joining process; (iv) the resulting temporal evolution and spatial distribution of the material microstructure throughout the weld region; and (v) spatial distribution of the as-welded material mechanical properties. In the present work, the GMAW-process model has been upgraded with respect to its predictive capabilities regarding the spatial distribution of the mechanical properties controlling the ballistic limit (i.e. penetration resistance) of the weld. The model is upgraded through the introduction of the sixth module in the present work in recognition of the fact that in thick steel GMAW weldments, the overall ballistic performance of the armor may become controlled by the (often inferior) ballistic limits of its weld (fusion and heat-affected) zones. To demonstrate the utility of the upgraded GMAW process model, it is next applied to the case of butt-welding of a prototypical high-hardness armor-grade martensitic steel, MIL A46100. The model predictions concerning the spatial distribution of the material microstructure and ballistic-limit-controlling mechanical properties within the MIL A46100 butt-weld are found to be consistent with prior observations and general expectations.

REPORT DOCUMENTATION PAGE (SF298)
(Continuation Sheet)

Continuation for Block 13

ARO Report Number   57228.30-EG
Ballistic-Failure Mechanisms in Gas Metal Arc W...

Block 13: Supplementary Note

Ballistic-Failure Mechanisms in Gas Metal Arc Welds of Mil A46100 Armor-Grade Steel: A Computational Investigation

M. Grujicic, J.S. Snipes, R. Galgalikar, S. Ramaswami, R. Yavari, C.-F. Yen, and B.A. Cheeseman

In our recent work, a multi-physics computational model for the conventional gas metal arc welding (GMAW) joining process was introduced. The model is of a modular type and comprises five modules, each designed to handle a specific aspect of the GMAW process, i.e.: (i) electro-dynamics of the welding-gun; (ii) radiation-/convection-controlled heat transfer from the electric-arc to the workpiece and mass transfer from the filler-metal consumable electrode to the weld; (iii) prediction of the temporal evolution and the spatial distribution of thermal and mechanical fields within the weld region during the GMAW joining process; (iv) the resulting temporal evolution and spatial distribution of the material microstructure throughout the weld region; and (v) spatial distribution of the as-welded material mechanical properties. In the present work, the GMAW process model has been upgraded with respect to its predictive capabilities regarding the spatial distribution of the mechanical properties controlling the ballistic-limit (i.e., penetration-resistance) of the weld. The model is upgraded through the introduction of the sixth module in the present work in recognition of the fact that in thick steel GMAW weldments, the overall ballistic performance of the armor may become controlled by the (often inferior) ballistic limits of its weld (fusion and heat-affected) zones. To demonstrate the utility of the upgraded GMAW process model, it is next applied to the case of butt-welding of a prototypical high-hardness armor-grade martensitic steel, MIL A46100. The model predictions concerning the spatial distribution of the material microstructure and ballistic-limit-controlling mechanical properties within the MIL A46100 butt-weld are found to be consistent with prior observations and general expectations.

1. Introduction

Our recently proposed multi-physics computational model for the conventional gas metal arc welding (GMAW) joining process (Ref 1-3), Fig. 1, is extended in the present work in order to enable predictions of the spatial distribution, throughout the weld, of the mechanical properties controlling the ballistic-limit. The welding process parameters were already correlated with the spatial distribution of the material microstructure and properties within the weld (consisting of the solidified weld pool, also referred to as the fusion zone, FZ, and the adjacent heat-affected zone, HAZ) using the original GMAW process model. However, regarding the prediction of the spatial distribution of the mechanical properties that control the ballistic limit in thick metallic-armor weldments, the model had serious limitations. Specifically, the model was unable to predict spatial distribution, throughout the weld, of the

following material properties: (a) material strength, (b) stiffness, (c) volume-based specific heat, (d) exponent of strain-hardening, (e) exponent of strain-rate sensitivity, and (f) material shear-strength temperature-dependence. In our previous work (Ref 1-3), the model was:

(a) applied to the GMAW of MIL A46100 (an air-quenchable, self-tempered, high-hardness, low-alloy martensitic, armor-grade steel). A summary of Johnson-Cook material-model parameters and other thermo-mechanical properties for this material is given in Tables 1 and 2; and

(b) validated by comparing the model predictions (regarding the spatial distribution of the material microstructure throughout the weld) with their experimental counterparts. In order to predict spatial distribution of the mechanical properties controlling the ballistic limit in welded-armor of this material, the extended GMAW process model is applied to the same steel grade in the present work.

The main objective of the present work is to improve the capability of our recently proposed GMAW process model to predict the spatial distribution of material properties within the weld region. This capability is important for two reasons. First, these properties may often be inferior relative to their base-metal counterparts. Second, the width of the weld in thick metallic-armor is often comparable to the armor thickness, and therefore may represent a significant portion of the armor exposed-surface area (Ref 4).

A concise summary of the multi-physics GMAW process model and its five modules, as reported in Ref 1-3, is presented

M. Grujicic, J.S. Snipes, R. Galgalikar, S. Ramaswami, and **R. Yavari**, Department of Mechanical Engineering, Clemson University, 241 Engineering Innovation Building, Clemson, SC 29634-0921; and **C.-F. Yen** and **B.A. Cheeseman**, Survivability Materials Branch, Army Research Laboratory, Proving Ground, Aberdeen, MD 21005-5069. Contact e-mail: gmica@clemson.edu.
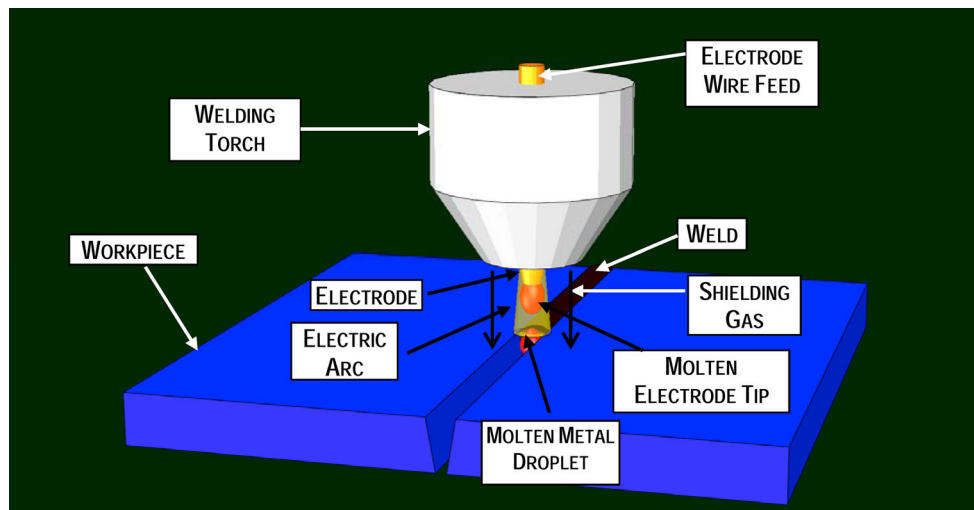
Fig. 1 A schematic representation of the conventional gas metal arc welding (GMAW) process

Table 1 Johnson-Cook strength model material parameters for MIL A46100

Parameter	Symbol	Units	Value
Young's modulus	E	GPa	205-215
Poisson's ratio	v	N/A	0.285-0.295
Reference strength	A	MPa	1000-1100
Strain-hardening parameter	B	MPa	250.0
Strain-hardening exponent	n	N/A	0.12
Strain-rate coefficient	C	N/A	0.02
Room temperature	T_{room}	K	298.0
Melting temperature	T_{melt}	K	1720
Temperature exponent	m	N/A	0.5

Table 2 General, thermo-mechanical, and thermal parameters for MIL A46100

Parameter	Symbol	Units	Value
Material mass density	ρ	kg/m^3	7840-7860
Coefficient of linear thermal expansion	α	1/K	11e-6-12e-6
Specific heat	C_p	J/kg K	440-520
Thermal conductivity	k	W/m K	35-50
Heat transfer coefficient	h	W/m^2 K	45
Sink temperature	T_{sink}	K	298
Emissivity	ε	N/A	0.57
Ambient temperature	T_{amb}	K	298

in section 2. In section 3.1, a brief overview is provided of the major changes made in the fifth module, the microstructure/property relationship module. Details related to construction of the sixth module, the ballistic-limit prediction module is presented in section 3.2. In the same section, the results pertaining to the spatial distribution of the ballistic limit throughout the weld in MIL A46100 steel are next presented and discussed. The main conclusions resulting from the present work are summarized in section 4.

2. Multi-physics GMAW Process Model

In order to help clarify the structure of the present six-module GMAW process model, a flowchart revealing the sequence and interconnectivity of the modules is depicted in Fig. 2. The first five modules were developed in Ref 1-3 and, hence, no summary of the key physical concepts and principles pertaining to these modules will be provided here. Instead, a few prototypical results yielded by these modules will be presented and discussed. The sixth module shown in Fig. 2 has been developed in the present work.

2.1 Welding-Gun Module

Figure 3(a) and (b) shows typical results of the temporal evolutions of the welding voltage (input) and the welding power (output), as yielded by this module. It should be noted that the output welding power shows considerable fluctuations even when the input welding voltage is set to a constant value.
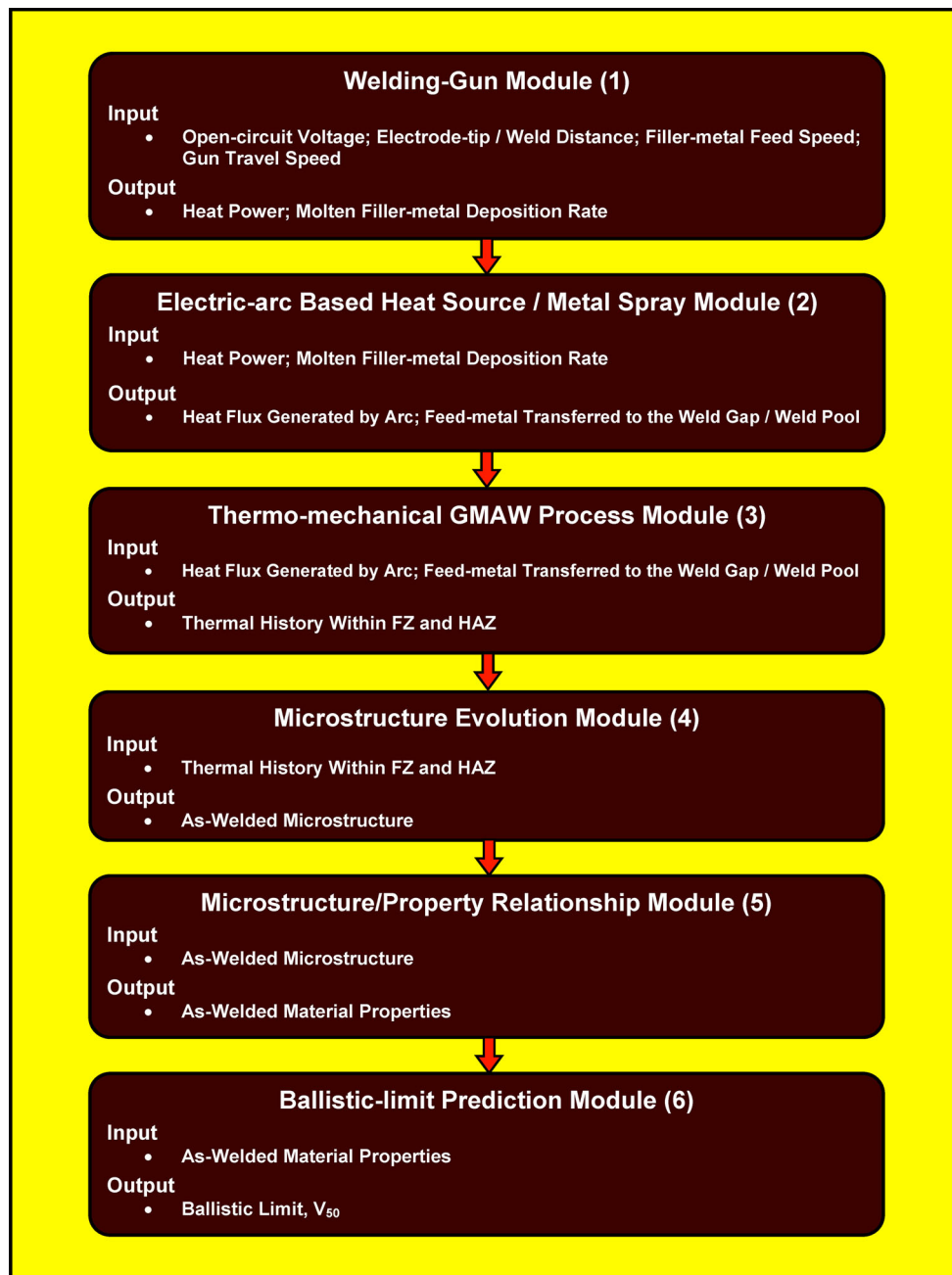
Fig. 2 The structure of the multi-physics GMAW process model consisting of six modules

Consequently, this module establishes the functional relationship between the input voltage and mean output power, and this functional relationship is subsequently passed to the next module.

2.2 Electric-Arc-Based Heat-Source/Metal-Spray Module

Figure 4 depicts a three-dimensional surface plot of normalized surface heat-flux as a function of distances along the weld transverse direction (x) and the weld longitudinal direction (y). It should be noted that x and y (as well as the standard-deviation of the assumed normal-circular power-density distribution function) are all normalized by the (equal transverse and longitudinal) workpiece half-edge lengths.

2.3 Thermo-mechanical GMAW Process Module

The results presented below were obtained for the case of MIL A46100 GMAW butt-welding.

2.3.1 Temporal Evolution of the Weldment Temperature Field. Typical results pertaining to the temporal evolution of the temperature field within the weld region over the (explicitly analyzed) right half of the weldment are depicted in Fig. 5(a)-(d), along with the coordinate system used in this analysis. The results shown in Fig. 5(a)-(d) are obtained at relative welding times of 0.6, 2.1, 3.6, and 4.8 s, respectively. The GMAW process parameters used to obtain these results are as follows: welding input voltage = 30 V, welding current = 200 A, electrode diameter = 1 mm, electrode-tip/weld distance = 1.3 cm,
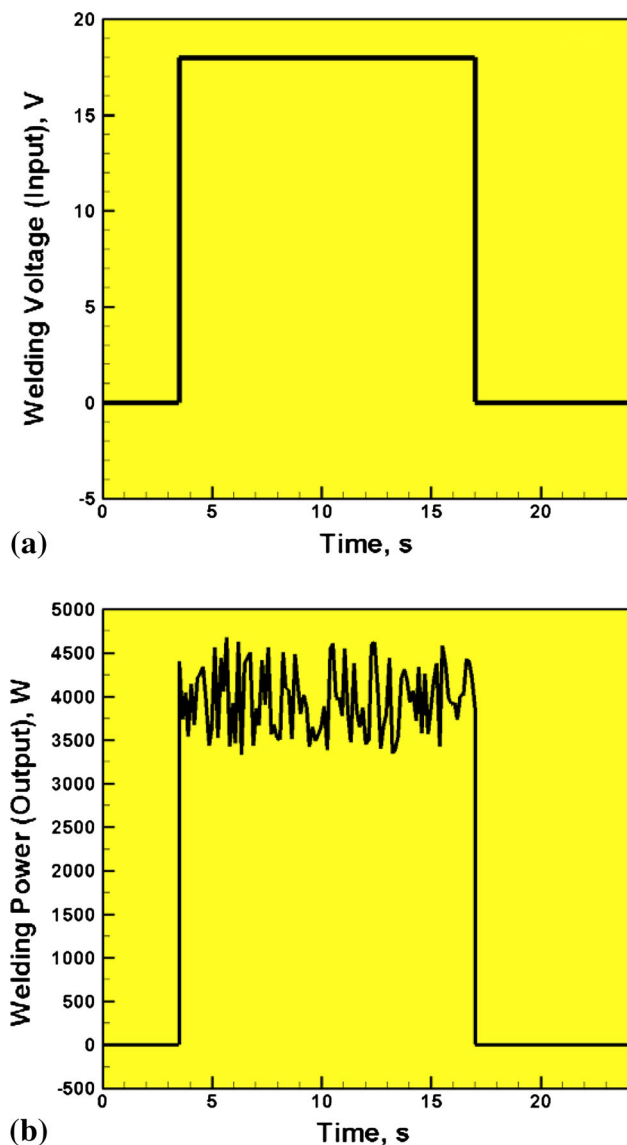
(a)

(b)

Fig. 3 Typical results yielded by the welding-gun module pertaining to temporal evolutions of (a) the input voltage; and (b) the output power

electrode feed-rate = 10 cm/s, and gun travel speed = 1 cm/s. It should be noted that regions of the weldment with a temperature exceeding the liquidus temperature (defined as the temperature at which the volume fraction of the liquid phase, during cooling from the melt, first begins to deviate from 100%) are displayed as red, for improved clarity.

Examination of the results displayed in Fig. 5(a)-(d) reveals that: (a) after a brief transient period, the FZ acquires a nearly constant size and shape as it travels along the welding direction (following the position of the weld gun); (b) as welding proceeds, the previously molten material within the FZ solidifies (and continues to cool) due to natural convection and radiation to the surroundings, together with conduction through the adjacent workpiece material region; and (c) under the aforementioned welding conditions, the FZ extends downward into the workpiece thickness by ca. 40-45%.

2.3.2 Temporal Evolution of Temperature Within the FZ and HAZ. Figure 6(a) and (b) shows typical results pertaining to the temporal evolution of temperature at fixed locations within the FZ and HAZ, respectively. Results pertaining to the weldment (through-the-thickness) mid-plane within the FZ are displayed in Fig. 6(a). In this figure, the distance of the material point in question from the weld y-z symmetry plane is denoted via the curve labels. Results pertaining to the weldment mid-plane within the HAZ, on the other hand, are displayed in Fig. 6(b). The curve labels used in this figure represent the distance of the material point in question from the FZ/HAZ interface. It should be noted that before the temperature-history results generated in this module are passed to the fourth (microstructure-evolution) module, they are computed for a larger number of closely spaced material points in the FZ and HAZ.

Examination of the results displayed in Fig. 6(a) and (b) reveals that:

(a) Temperatures in excess of the MIL A46100 liquidus temperature (1772 K), are experienced by material points which reside within the FZ. As a result of the arrival of the weld gun, these points are subjected to a steep rise in temperature, which is followed by a relatively steep drop in temperature due to the subsequent departure of the weld gun; and

(b) Temperatures which are in excess of the MIL A46100 Ac_1 (defined as the highest temperature at which austenite is still present during cooling) temperature (982 K), but which are lower than the MIL A46100 liquidus temperature, are experienced by material points which reside within the HAZ. These points spend more time at temperatures near the peak temperature, are subjected to a significantly lower heating rate and undergo relatively slow cooling.

2.3.3 Thermal-Strain/Residual-Stress Fields. High thermal stresses and, in turn, plastic deformation (permanent distortion) can occur in the weld region if non-uniformity in the temperature distribution throughout this region is sufficiently large. In particular, due to highly non-uniform input thermal flux (as seen in Fig. 4), the FZ may experience high thermal stresses that lead to eventual plastic deformation. This would cause weldments to acquire residual stresses upon cooling to room temperature. As explained earlier, the present multi-physics GMAW process model, due to its thermo-mechanical character, is capable of predicting the development of such welding-induced permanent distortions and residual stresses. Figure 7(a) and (b) shows typical thermal-strain/residual-stress results obtained using the present rendition of the thermo-mechanical GMAW process module (Ref 5-13). Spatial distribution of the equivalent plastic strain and the von Mises equivalent residual stress, over a transverse section of the weld, are depicted in Fig. 7(a) and (b), respectively. Instead of displaying the contour-level legends, the maximum values of the equivalent plastic strain and the von Mises equivalent residual stress are denoted in these figures, for improved clarity. Examination of the results displayed in Fig. 7(a)-(b) show that the largest plasticity/residual-stress effects are observed within the FZ and the adjacent portions of the HAZ, as is to be expected.

Welding-induced permanent distortions may affect functional performance of a weldment, due to the associated shape
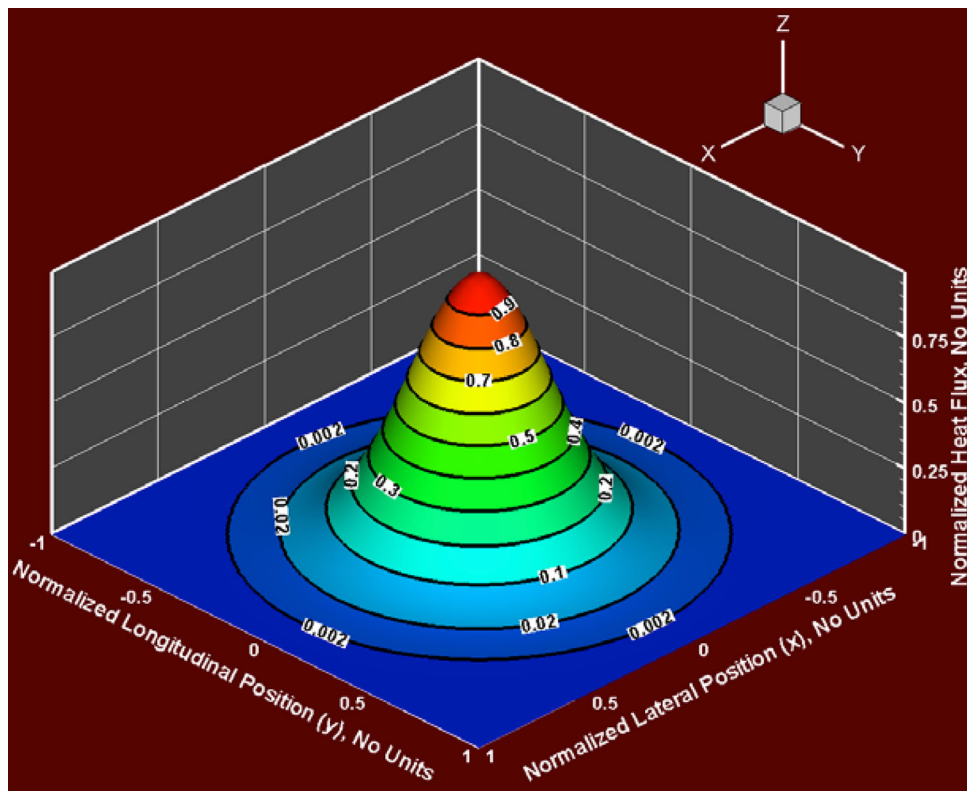
Fig. 4 A normalized heat-flux three-dimensional surface plot (for the case of the circular-normal distribution) as a function of the lateral and longitudinal locations (normalized by the corresponding workpiece half-edge lengths) on the workpiece top surface. The $x = y = 0$ location, associated with the maximum heat-flux, corresponds to the current position of the electrode axis

and dimensional changes, while the presence of the (tensile) residual stresses may degrade structural performance and/or affect reliability/durability of the weld. In addition, through the so-called "deformation-induced" and "stress-assisted" transformation effects (e.g., Ref 14), plastic strains and residual stresses may affect the progress of the austenite → bainite and austenite → martensite displacive phase transformations. These phase transformations will be presented in greater detail in the section dealing with the microstructure-evolution (fourth) module. These effects are not included in the current rendition of the microstructure-evolution module, even though they may somewhat influence the predictions of the microstructure distribution within the weld. However, as demonstrated in Ref 1, within the common GMAW process parameter envelope, the role of these effects is relatively small and, hence, this is presently not considered as a major issue in the current module.

2.4 Microstructure-Evolution Module

Figure 8(a)-(f) depicts typical results yielded by the microstructure-evolution module, for MIL A46100 that is initially in the as-hot-rolled and self-tempered martensitic state. These results are obtained under the following GMAW process conditions: input welding voltage = 30 V, welding current = 200 A, electrode diameter = 1 mm, electrode-tip/weld distance = 1.3 cm, electrode feed-rate = 10 cm/s, and gun travel speed = 1 cm/s. Figure 8(a)-(e) shows the spatial distributions, over a transverse section of the weld and the workpiece region adjacent to the weld, of the volume fractions for the following phases: (a) allotriomorphic ferrite, (b) Widmanstatten ferrite, (c) bainite, (d) freshly formed martensite, and (e)

tempered martensite, respectively. The corresponding spatial distribution of the prior-austenite grain size is shown in Fig. 8(f).

Examination of the results displayed in Fig. 8(a)-(f) reveals that:

(a) The FZ consists only of allotriomorphic ferrite and Widmanstatten ferrite, Fig. 8(a)-(b). This observation is to be expected, considering the fact that the material within this region is initially subjected to temperatures significantly higher than the material liquidus temperature and, hence, is associated with a long cooling time. Furthermore, since austenite chemical composition is nearly identical to that of the alloy itself, the material within the FZ possesses relatively low hardenability (the ease of transformation of austenite into martensite);

(b) There is a fairly small (less than 30 vol.%) volume fraction of freshly formed martensite within the FZ, Fig. 8(d). This finding is fully consistent with the fact that the weld region experiences relatively low cooling rates and contains austenite with relatively low hardenability. Upon crossing the FZ/HAZ interface and entering the HAZ, the volume fraction of freshly formed martensite first increases (to a value in excess of 85 vol.%) and then decreases (to a value of ca. 10 vol.%). The volume fraction of the freshly formed martensite subsequently drops to zero upon crossing the HAZ/unaffected-material boundary. A compromise between the amount of austenite available to transform into martensite and the hardenability of austenite is responsible for the spatial distribution of the volume fraction of freshly

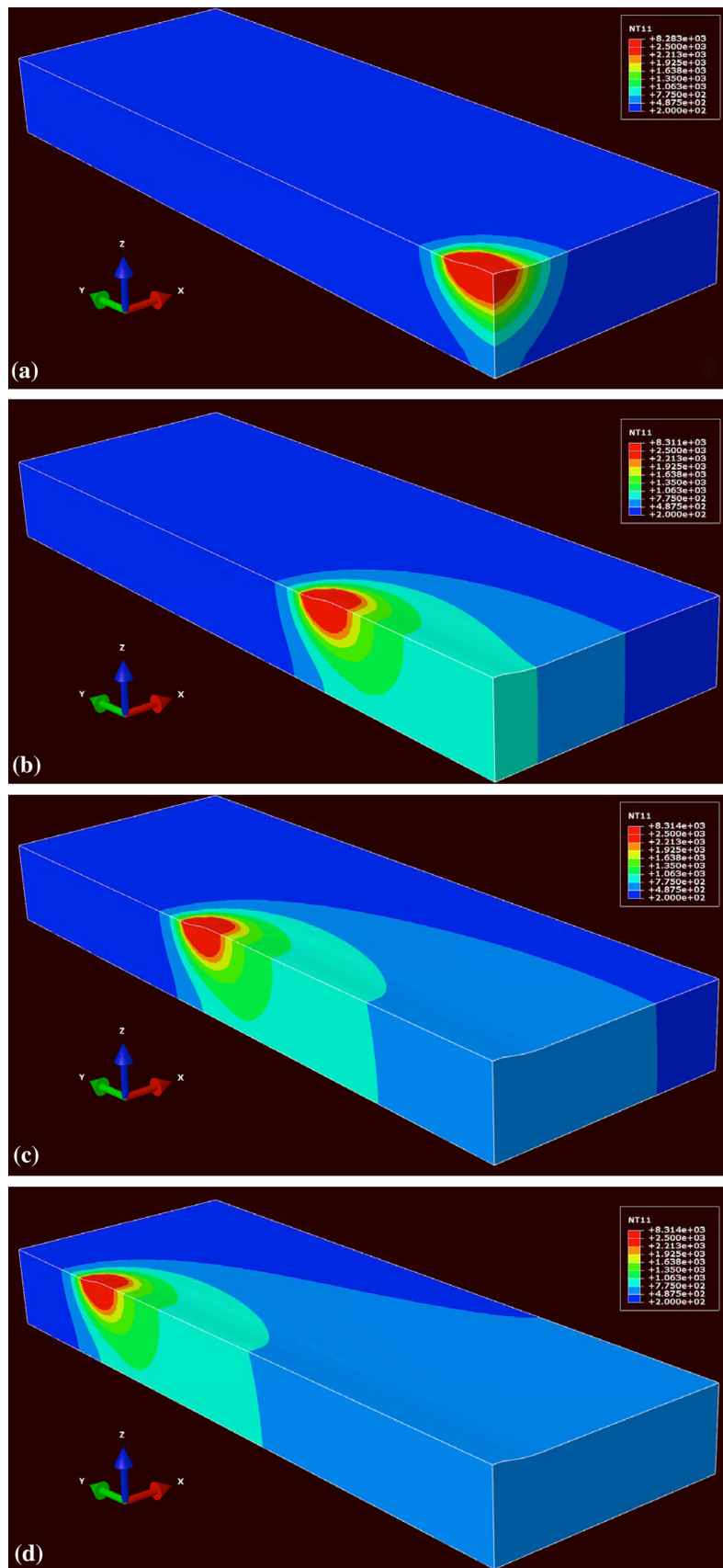**Fig. 5** Spatial distribution of the temperature field in the weld region over the (analyzed) right-portion of the MIL A46100 weldment at welding times of (a) 0.6 s, (b) 2.1 s, (c) 3.6 s, and (d) 4.8 s under the following welding conditions: welding input voltage = 30 V, welding current = 200 A, electrode diameter = 1 mm, electrode-tip/weld distance = 1.3 cm, electrode feed-rate = 10 cm/s, and gun travel speed = 1 cm/s
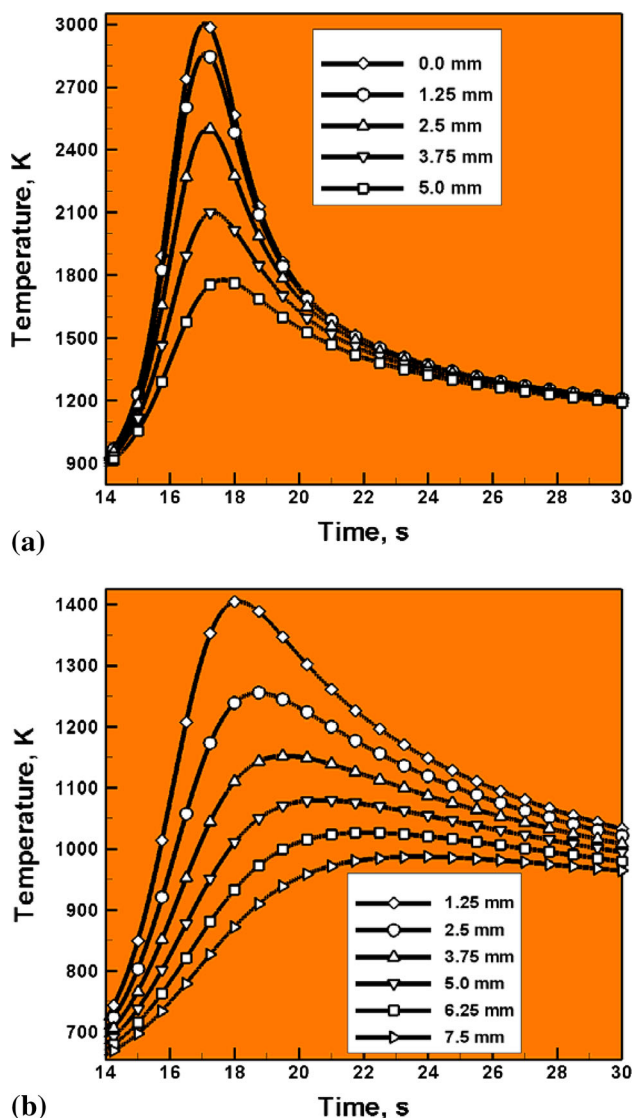
Fig. 6 Temporal evolution of temperature: (a) along the workpiece mid-plane within the FZ (the curve labels denote the distance of the subject material point from the weld *y-z* symmetry plane); and (b) along the workpiece mid-plane within the HAZ (the curve labels denote the distance of the subject material point from the HAZ/FZ interface)

formed martensite. Specifically, it is assumed that full austenitization takes place in the HAZ regions which were exposed to temperatures above Ac_3 (defined as the highest temperature at which α-ferrite forms during cooling), but this austenite possesses low hardenability. On the other hand, austenitization becomes incomplete as one enters the intercritical region, within which the maximum exposure temperature is between Ac_1 and Ac_3. However, the attendant austenite possesses higher hardenability. Consequently, the volume fraction of the freshly formed martensite first increases (due to the dominating effect of the increased austenite hardenability), then passes through a peak value and finally decreases (due to a lower volume fraction of austenite available for transformation to martensite) as the maximum exposure temperature decreases from Ac_3 to Ac_1. Below a maximum exposure temperature corresponding

to Ac_1, no austenitization takes place during heating and, therefore, austenite → (freshly formed) martensite phase transformation takes place;

(c) Variation of the volume fraction of bainite throughout the FZ and within the HAZ (as a function of distance from the FZ/HAZ interface), Fig. 8(c), is merely a reflection of the competition between the austenite → bainite phase transformation and the austenite → (freshly formed) martensite phase transformation;

(d) Tempered martensite does not occur in the FZ, or within the fully austenitized portion of the HAZ, Fig. 8(e). In the remainder of the HAZ, tempered martensite volume fraction increases with increasing distance from the FZ/HAZ interface. Tempered martensite is the only phase found in regions of the HAZ with a maximum exposure temperature of Ac_1; and

(e) Moving from the HAZ/unaffected-material boundary, the grain size first continuously increases from its initial value (40 μm), to a value of ~80 μm near the HAZ/FZ interface, Fig. 8(f). Within the FZ, the grain size first experiences a slight drop (the "chill-zone" effect) and then continues to increase towards the final value of ~70 μm.

2.5 Microstructure/Property Relationship Module

As part of the present work, the microstructure/property relationship module has been upgraded in order to impart to the GMAW process model capabilities for the prediction of material strength distribution within the weld. This upgrade utilizes the following three-step procedure: (a) first, the key contributions to the material strength within different portions of the weld zones are identified, and the governing equations for the corresponding strengthening mechanisms are assembled and parameterized; (b) next, a superposition scheme is developed which will assess the combined effect of different strengthening mechanisms; and (c) finally, a functional relationship is established between the material strength and hardness in order to predict the spatial distribution of the material hardness within the weld region. This can then be used to validate the multi-physics GMAW process model by comparing the computed material hardness distribution with its experimental counterpart. Such validation is carried out in the portion of this subsection entitled "Typical Results."

2.5.1 Main Contributors to the Weld-Material Strength. To identify the following main strength contributors in prototypical armor steels like MIL A46100, the crystal structure, chemical composition, internal substructure, and external morphology of the attendant phases/micro-constituents are analyzed. This analysis revealed the following main strengthening mechanisms: (a) intrinsic (i.e., Peierls barrier control) strength of the phases/micro-constituents; (b) solid-solution strengthening; (c) alloy-carbide/cementite precipitation hardening; (d) dislocation substructure-based strengthening; and (e) strengthening by grain boundaries and phase interfaces. A brief overview of key phenomena/processes pertaining to these strengthening mechanisms and the governing functional relationships will be provided in the remainder of this section.

Intrinsic Strength of the Phases/Micro-constituents. Atomic-scale friction experienced by the gliding dislocations during plastic deformation is the main contributor to the intrinsic strength of each phase/micro-constituent (Ref 15).
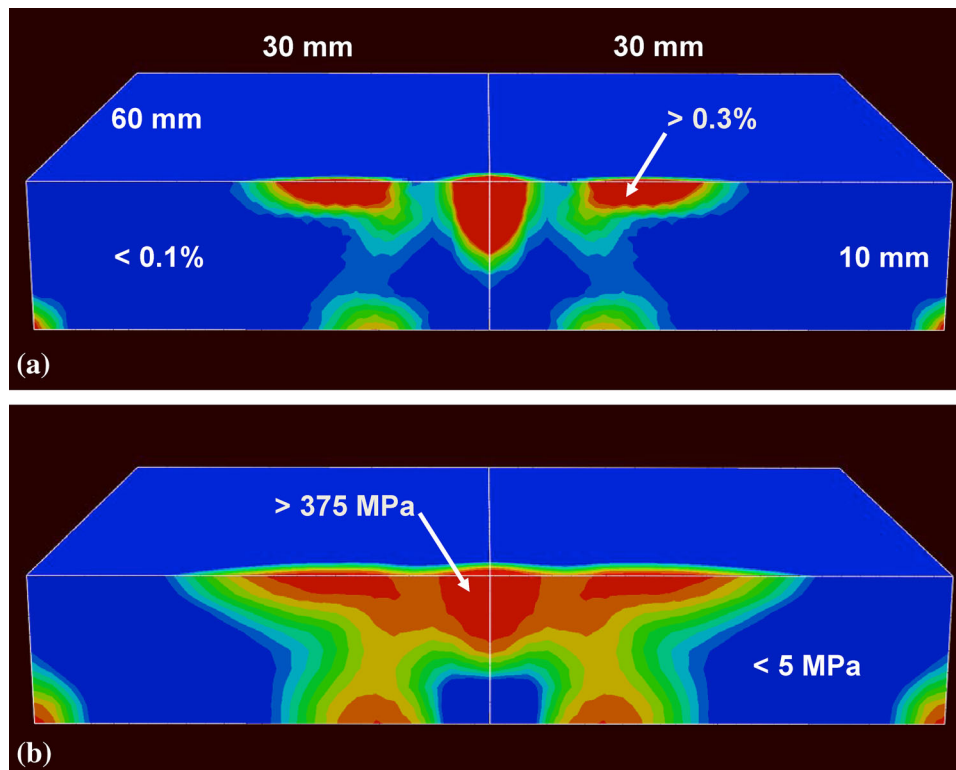
Fig. 7 Spatial distribution of (a) equivalent plastic strain; and (b) residual von Mises equivalent stress over a transverse section of the weld and the workpiece region adjacent to the weld

Solid-Solution Strengthening. The elastic (size and modulus mismatch type of) interactions between the solute atoms and dislocations are assumed to be the main controlling factor for solid-solution strengthening (Ref 16). The contribution of this mechanism to the material strength is assessed using the statistical approach of Labusch (Ref 17), which accounts for the distribution of the atom/dislocation interaction forces and distances. This approach enables evaluation of the increase in the critical resolved shear stress, due to the dislocation/solute-atom interactions, required for dislocation glide.

Alloy-Carbide/Cementite Precipitation Hardening. Gliding dislocations experience increased resistance as a result of their interactions with precipitates, which leads to precipitation hardening. The key factors that control the extent of precipitate hardening include precipitate size, volume fraction, number density, and chemical/mechanical properties, as well as the state of coherency at the precipitate/matrix interfaces. Two mechanisms, by which gliding dislocations generally overcome precipitates, are (a) precipitate shearing/cutting, a process which increases precipitate/matrix interfacial area and leads to the formation of interfacial ledges, stacking faults, and anti-phase boundaries (in the case of ordered crystalline precipitates); and (b) by looping around the precipitates, a process which leaves behind precipitates surrounded by dislocation loops and increases the effective size of the precipitates. Increases in the size of the precipitates leads to increases in the critical resolved shear stress required for precipitate shearing. However, for a given volume fraction of precipitate, the critical resolved shear stress required for precipitate-bypass via the looping mechanism decreases with an increase in the precipitate size. Consequently: (a) the extent of precipitation hardening for

small precipitates is controlled by precipitate shearing; (b) precipitate hardening at large precipitate sizes is controlled by dislocation looping around the precipitates; and (c) there exists a critical precipitate size, at which, the extent of precipitate hardening is the highest. The degree of precipitate hardening associated with the shearing process is dependent on the nature and the extent of phenomena/processes (e.g., precipitate/matrix interfacial energy, character/magnitude of the stress-free eigen-strain of coherent precipitates, the extent of precipitate/matrix elastic-modulus mismatch, the stacking fault energy, the anti-phase boundary energy, etc.) responsible for the resulting increase in the critical resolved shear stress necessary for dislocation glide. The shearing mode of the precipitate hardening process is expected to be controlled by the elastic-modulus mismatch between the matrix and the precipitates. This is due to the fact that incoherent alloy-carbide/cementite precipitates are primarily found in MIL A46100. Consequently, the magnitude of the matrix/precipitate elastic-modulus mismatch is assumed to be the key contributor to the associated increase in the critical resolved shear stress for dislocation glide. The critical resolved shear stress required for precipitate-bypass by the looping mechanism is quantified using the Orowan-Ashby approach (Ref 18). This approach is based on the assessment of the stress required to bend a dislocation segment into a semi-circular shape having a radius equal to the precipitate half-distance along the dislocation line.

Dislocation Substructure-Based Strengthening. Plastic relaxation takes place, both within the growing martensitic phase and within the neighboring austenite phase, due to a large shape change (i.e., lattice-invariant shear strain) that accompanies austenite $\rightarrow$ martensite phase transformation. This results in a
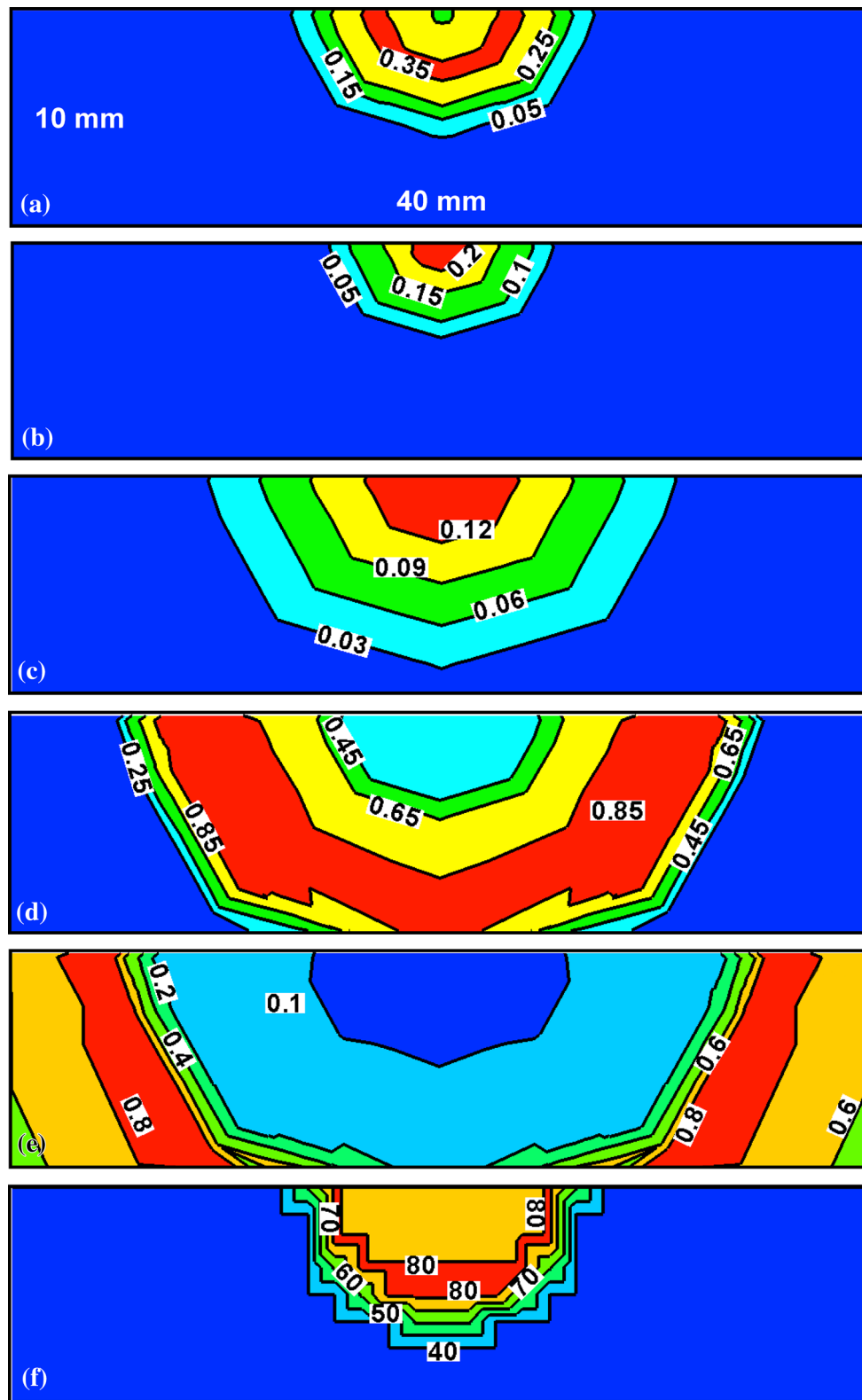
Fig. 8 Spatial distribution of phase volume fractions for (a) allotriomorphic ferrite, (b) Widmanstatten ferrite, (c) bainite, (d) freshly formed martensite, (e) tempered martensite, and (f) grain size (in μm) over a transverse section of the weld and the workpiece region adjacent to the weld

large occurrence of dislocations in freshly formed martensite, which act as glide-obstacles to other dislocations. Therefore, dislocation glide requires an increase in the critical resolved shear stress and, hence, an increase in material strength. The extent of this strengthening is a function of the transformation temperature since this temperature affects the strength of, and

the extent of plastic relaxation in, the transforming austenite. To quantify this strengthening mechanism: (a) first, the approach of Takahashi and Bhadeshia (Ref [19]) is employed in order to establish a functional relationship between the transformation-induced dislocation density, ρ, and the transformation temperature, T; (b) then, the approach of Keh and Weissman (Ref [20]) is utilized to correlate the increase in critical resolved shear stress with the increase in transformation-induced dislocation density; and (c) finally, the approach of Leslie et al. (Ref [21]) is used to assess the effect of tempering, which causes dislocation-rearrangement/recovery/partial-annihilation.

Strengthening by Grain Boundaries and Phase Interfaces. Grain boundaries and phase interfaces are fundamentally different crystalline defects in comparison to the previously analyzed obstacles to dislocation glide (i.e., substitutional/interstitial alloying atoms, precipitates, and "forest" dislocations). This difference stems from the fact that grain boundaries and phase interfaces act as impenetrable barriers to dislocation glide. Consequently, during plastic deformation, dislocations tend to pile-up at these boundaries and interfaces. The subsequent spread of plastic deformation depends on the nucleation and glide of dislocations in the adjacent grains/phase-particulates (promoted by the stress-concentration effects arising from the dislocation pile-ups). Simple mechanics analysis of the dislocation/boundary interactions reveals that the larger the grain/phase-particulate size, the larger is the dislocation pile-up that can be accommodated, the larger are the pile-up-induced stress-concentration effects and, hence, the lower is the applied stress at which new dislocations are nucleated. In other words, material strength decreases with an increase in the grain/phase-particulate size. In the microstructure/property relationship module, this effect is included using the Hall-Petch relation (Ref [22]). Due to the complex multi-phase nature of MIL A46100, one can expect different grain boundaries and phase interfaces in MIL A46100 (e.g., prior-austenite grain boundaries, martensite lath boundaries, bainitic sheave boundaries, and the associated two-phase interfaces). For all of these, it is assumed that the Hall-Petch relationship is valid.

2.5.2 Strength Superposition. In this section, an approach is proposed for combining contributions of the strengthening mechanisms, identified above, to the total local material strength within the weld. The approach involves the following steps:

(a) first, it is recognized that the intrinsic (i.e., Peierls barrier control) strengthening mechanism provides the baseline level of the material strength while the remaining four strengthening mechanisms provide the respective increments in the material strength (as quantified by their respective critical resolved shear strengths for dislocation glide);

(b) to obtain the total local material strength within a crystalline phase, the contributions of the latter four strengthening mechanisms are superposed and then added to the base-material strength; and

(c) the superposition principle is employed in the following way: (i) for mechanisms operating at the same length scale (e.g., solid-solution strengthening effects associated with different alloying elements), the square roots of the corresponding critical resolved shear-strength increments

are first summed and then squared (Ref [15]); and (ii) for mechanisms operating at different length scales (e.g., solid-solution strengthening and precipitation hardening), a simple linear-superposition of the corresponding critical resolved shear-strength increments is used.

The procedure described above yields the total critical resolved shear stress for dislocation glide (i.e., the material shear strength). To obtain the material normal strength, the material shear strength is multiplied by a factor, $\sqrt{3}$, in accordance with the von Mises yield function.

It should be noted that the superposition procedure described above can yield the strength of each of the possible crystalline phases present at a given location within a steel weld. However, the local weld microstructure typically does not consist of a single phase but rather involves a number of coexisting phases. The volume fraction of each of these phases is predicted by the microstructure-evolution module. To obtain the total local strength at a multi-phase location within the weld, a simple rule-of-mixtures is employed within the present module.

2.5.3 Strength Versus Hardness Relationship. The superposition methods described above can be used to predict the normal strength at a given material point within the weld. The resulting spatial distribution of material strength within the weld can be used to assess the overall structural performance of the weldment. However, the knowledge of the material strength distribution cannot be generally used to validate the multi-physics GMAW process model. This validation would simply require fabrication and testing of a large number of micron-sized tensile/compression specimens. More frequently, it is a common practice to use a distribution of indentation hardness (or, more precisely, micro/nano-hardness) over the transverse (or some other) section of the weldment, to characterize the distribution of mechanical properties throughout the weld region. Since the microstructure/property prediction module yields the spatial distribution of the material strength while experimental data typically pertain to the spatial distribution of the material hardness, it is necessary to establish the strength-to-hardness conversion relation before this portion of the GMAW process model can be validated.

Ashby and Jones (Ref [23]) suggested that material hardness (expressed in the same units as the normal strength) can be calculated by multiplying the normal strength by a factor of 3.0. However, Vickers micro-hardness tests typically quantify material hardness in terms of the so-called Vickers hardness number (VHN) which is the material hardness expressed in units of kgf/mm^2. To obtain VHN, the material hardness, expressed in MPa, should be divided by a factor of 9.81.

2.5.4 Typical Results. Figure 9(a) shows the spatial distribution of the MIL A46100 VHN within the weld region, obtained under the same GMAW process and base-/filler-metal conditions as the results presented in Fig. 8(a)-(f). The results displayed in Fig. 9(a) show that: (a) the hardness of the material within the FZ (the as-cast microstructure of which is dominated by allotriomorphic and Widmanstatten ferrite) is lowered relative to the hardness of the as-received material, VHN = 750; (b) the hardness within the (previously mentioned) "intercritical region" is substantially higher than that of the as-received material; and (c) in general, both the low-hardness and high-hardness regions have to be critically examined since they lead to negative consequences. That is, the low-hardness region is expected to compromise the load-
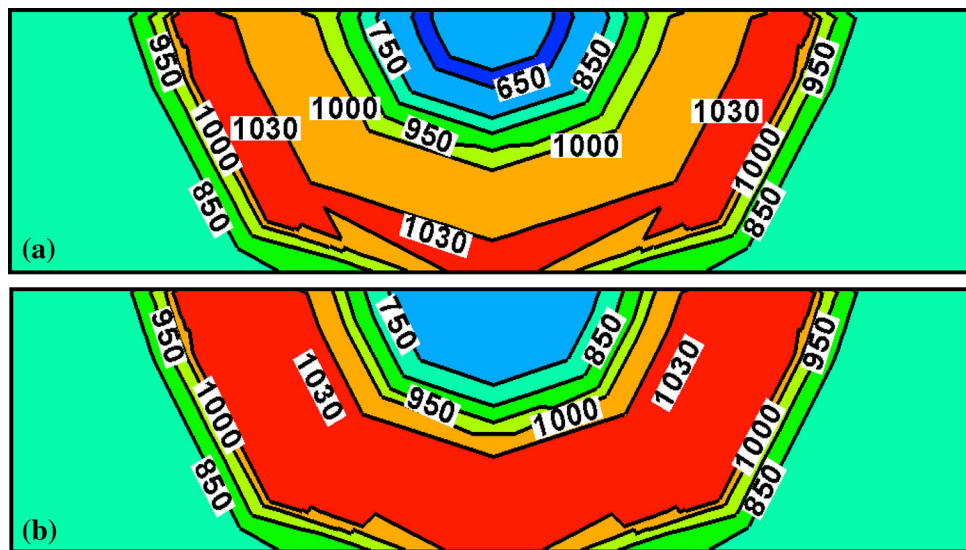
Fig. 9 Typical spatial distribution of the material VHN hardness within the weld region of MIL A46100 as: (a) computed in the present work; and (b) as reconstructed using the results reported in Ref 31

bearing capacity of the weldment while the high-hardness region, through the accompanying loss of toughness/ductility, may compromise weldment reliability/durability.

In the remainder of this section, an attempt is made to validate the microstructure/property relationship module. Toward that end, the results displayed in Fig. 9(a) are compared with their experimental counterparts (reported in Ref 24 and recreated) in Fig. 9(b).

A comparison of the results depicted in Fig. 9(a) and (b) reveals that:

(a)   in the HAZ regions which are located further away from the FZ/HAZ interface, the agreement between the two sets of results is reasonable; and

(b)   on the other hand, some differences in the two sets of results are observed in the remainder of the weld region. These differences can be attributed to the fact that, while in the present work the base and the filler-metal chemistries are identical, in Ref 24 the chemical composition of the filler-metal was somewhat different from that of the base-metal. Hence, within the FZ and the region of the HAZ adjacent to the FZ within which solid-state diffusion was active, the weld chemistry was different for the results displayed in Fig. 9(a) and (b).

3. Upgrade of the GMAW Process Model

The main objective of the present work, as stated earlier, involves: (a) improving the predictive capability of the model relative to the mechanical properties controlling the ballistic-limit/penetration-resistance; and (b) imparting ballistic-limit prediction capabilities to the model. In the remainder of this section, these two aspects of the GMAW process model upgrade are discussed separately. In the present work, the ballistic-limit, for a specific ballistic-impact scenario, is quantified using the velocity parameter V_{50}. V_{50} is defined as the

projectile incident-velocity at which the likelihood of target penetration is 50%.

3.1 Upgrade of the Microstructure/Property Relationship Module

As mentioned earlier, the microstructure/property relationship module was originally capable of predicting strength/hardness of different phases and the overall material strength/hardness distribution throughout the weld. For calibrating and validating the GMAW process model against the available experimental data, these predictive capabilities are highly critical. With respect to predicting the ballistic-limit distribution throughout the weld, however, these capabilities are insufficient. These shortcomings of the original microstructure/property relationship module are addressed in the present work by imparting to the model the capabilities of predicting the weld-spatial distributions of the following material properties: (a) stiffness, (b) volume-based specific heat, (c) exponent of strain-hardening, (d) exponent of strain-rate sensitivity, and (e) material shear-strength temperature-dependence. It should be noted that for complete validation of the upgraded microstructure, one should validate the model predictions using the appropriate experimental measurements. This is a formidable task since the material properties in question can substantially vary throughout the weld region. Consequently, experimental validation of the present model would require testing of a large number of micron-sized specimens extracted from different portions of the weld, and was considered to exceed the scope of the present work. It should be noted that work is underway to provide experimental validation of the upgraded microstructure/property relationship module. However, in this work a simpler steel grade is being used to reduce the extent of experimental effort needed.

The physical and mathematical meanings of the material properties (c)-(e), mentioned above, will be provided in the next subsection. In addition, an attempt will be made in the next subsection to demonstrate that the spatial distributions of these material properties must be known in order to predict the

ballistic limit and its spatial distribution throughout the weld. In the remainder of this subsection, brief descriptions will be provided of the procedures used to assess the aforementioned five material properties.

Material Stiffness: The material stiffness properties of steels (and their constituent phases) are typically considered as being isotropic and microstructure-insensitive. Following this assumption, typical (constant) values are assigned to the Young's modulus (210 GPa) and Poisson's ratio (0.3) (Ref 25) in the present work.

Volume-Based Specific Heat: The volume-based specific heats of steels (and their constituent phases) are also generally assumed to be isotropic and microstructure-insensitive. Consequently, a typical (constant) value for the volume-based specific heat (3.7 MJ/m^3 K) is used (Ref 25) in the present work.

Exponent of Strain-Hardening: The exponent of strain-hardening is generally considered to be a microstructure-sensitive material property. In addition, this property is assumed to be inversely related to the material strength/hardness (Ref 26). Figure 10 shows the functional relationship between the material yield strength and its exponent of strain-hardening for MIL A46100 derived in the present work.

Exponent of Strain-Rate Sensitivity: While the exponent of strain-rate sensitivity is generally found to be moderately sensitive to the material microstructure, it is assumed to be constant within the weld (primarily due to a lack of the relevant high-strain-rate data for different crystalline phases and micro-constituents within the weld). The procedure recently proposed in Ref 13 was utilized to determine a mean exponent of strain-rate sensitivity throughout the weld, and yielded a strain-rate sensitivity exponent of 0.005 for MIL A46100 steel. Since this value is relatively low in comparison to the value of exponents of strain-rate sensitivity found in most metals, MIL A46100 can be considered as a weakly strain-rate-dependent material.

Material Shear-Strength Temperature-Dependence: The material shear-strength temperature-dependence is generally found to be a microstructure-dependent property. Unfortunately, there is a lack of relevant experimental high-temperature data for this property in different crystalline phases and micro-constituents within the weld. Consequently, and following the

procedure outlined in Ref 1-3, this property was assumed to take on different constant values within the FZ and HAZ. To assess the mean values of the material shear-strength temperature-dependence within the two weld-zones, a procedure based on thermally activated glide of dislocations within the representative microstructures of the two weld-zones, originally proposed in Ref 15, was employed in the present work. Within the FZ and HAZ of MIL A46100, this procedure yielded the (room temperature) shear-strength temperature-dependence values of −0.17 and −0.15 MPa/K, respectively. The lower magnitude of the shear-strength temperature-dependence in the HAZ can be attributed to the operation of auto-tempering processes within this region. As far as the (room temperature) shear strength of the subject material MIL A46100 is concerned, its as-received value of 577 MPa has been taken from Ref 4. On the other hand, within the weld, the results obtained in the present work revealed that the (room temperature) shear strength varies in an approximately 500-650 MPa range.

3.2 Creation of the Ballistic-Limit Prediction Module

The procedure used to construct the sixth (ballistic-limit prediction) module of the GMAW process model includes the following steps: (a) identification of the failure mechanisms controlling the ballistic limit; (b) for each of the failure mechanisms identified, a physically based model is developed to predict the associated ballistic limit; (c) the associated governing equations and their parameterizations are next incorporated into the sixth module; and (d) last, the sixth module is utilized to predict the spatial distribution of the ballistic limit within a GMAW joint in MIL A46100.

3.2.1 Identification of the Ballistic-Limit-Controlling Failure Mechanisms. Based on a review of the public-domain literature conducted as part of the present work, the following main failure modes controlling the ballistic limit in metallic welds were identified (Ref 27-30): (a) front/impacted and back/rear face petaling, Fig. 11(a) and (b); (b) ductile hole-enlargement, Fig. 12; (c) plugging, Fig. 13; and (d) spalling, Fig. 14(a) and (b). Both the weld factors (e.g., weld soundness/quality, relative and absolute sizes of the FZ and HAZ, weld microstructure, spatial distribution and type of microstructure within the weld, etc.) and the impactor properties (e.g., projectile's mass, shape, size (relative to the target thickness), and hardness (relative to that of the target-material)) have been found to control the dominant failure mode in a specific ballistic-impact scenario. Since detailed descriptions of the key features of the aforementioned four failure mechanisms can be found in Ref 27-30, the same details will not be presented here.

3.2.2 Modeling of the Failure Mechanisms. This subsection focuses on assembling the relations quantifying the contribution of the four failure modes to the target ballistic limit.

Front/Impacted and Back/Rear Face Petaling: Since this mode of failure makes a small overall contribution to the ballistic limit of thick armor-plates (Ref 31), the role of this failure mechanism in the overall ballistic performance of GMAW-joints was not modeled and/or assessed in the present work.

Ductile Hole-Enlargement: To model this failure mechanism, the so-called "Cavity Expansion Theory (CET)" (Ref 29, 30, 32-34) is employed here. This theory treats target penetration by a (rigid, ogive-nosed) projectile as a problem of radial expansion of the associated (cylindrically shaped) cavity within
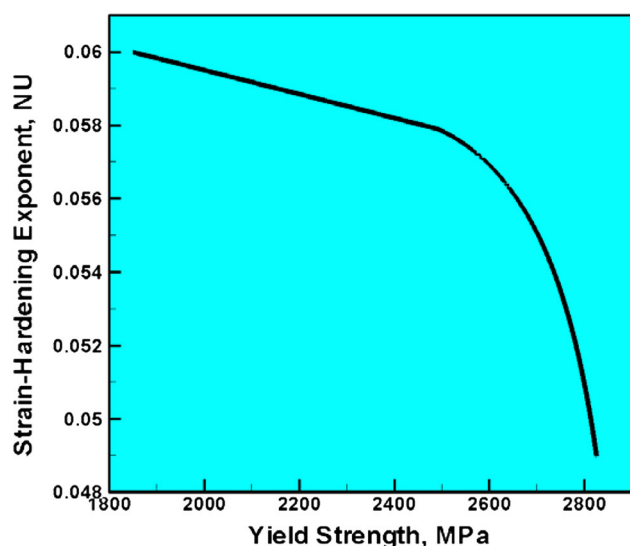

Fig. 10 Derived functional relationship between the material yield strength and its strain-hardening exponent for MIL A46100
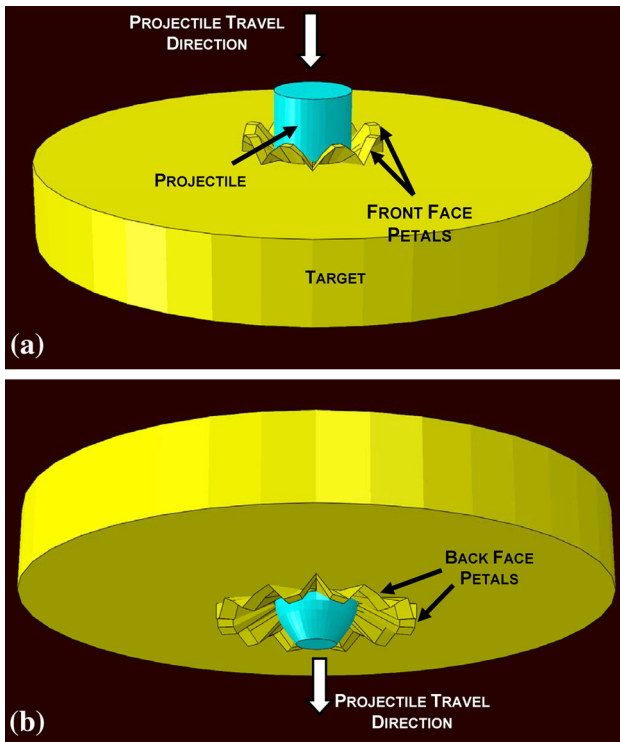
Fig. 11 Schematic representation of (a) front face; and (b) back face petaling failure mechanism
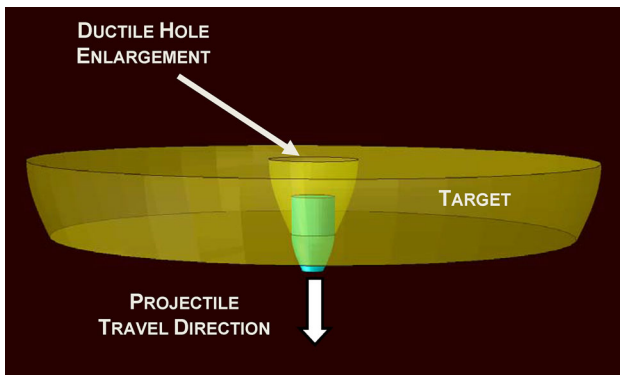

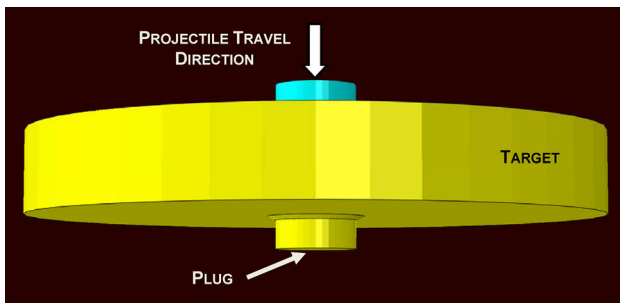**Fig. 12** Schematic representation of the ductile hole-enlargement failure mechanism

Fig. 13 Schematic representation of the plugging-failure mechanism

the target. To derive the ballistic-limit relation, the following three-step procedure is employed: (a) the governing mass and momentum conservation equations are first combined with the elastic-plastic material constitutive relations for the target, to establish a functional relation between the axial force opposing target penetration and the cavity-expanding radial stress (σ_s); (b) the latter quantity, σ_s, is next correlated with the target-material stiffness and strength (including strain-hardening) parameters and with the cavity expansion rate; and (c) by employing Newton's second law, and by ignoring the contribution of the radial expansion inertia to σ_s, the ballistic limit V_{50} is defined as the projectile minimal incident-velocity required for the projectile to traverse the entire target thickness, and expressed as (Ref 35):

$$V_{50} = \left(\frac{2\pi a^2 h \sigma_s}{m}\right)^{1/2}, \qquad \text{(Eq 1)}$$

where a is the projectile shank radius, m the projectile mass, and h the target thickness.

For a nonlinear strain-hardening target-material with the post-yield uniaxial stress, σ_u versus uniaxial strain ε_u relation being defined as:

$$\sigma_u = Y\left(\frac{E\varepsilon_u}{Y}\right)^n, \qquad \text{(Eq 2)}$$

where Y is the quasi-static yield strength, E is Young's modulus, and n is the strain-hardening exponent, σ_s can be expressed as

$$\sigma_s = \frac{Y}{\sqrt{3}}\left(1 + \left[\frac{E}{\sqrt{3}Y}\right]^n \int_0^b \frac{(-\ln x)^n}{(1-x)}dx\right), \quad b = 1 - \frac{\sqrt{3}Y}{E}. \qquad \text{(Eq 3)}$$

Equations 1 and 3 are then combined to obtain:

$$V_{50} = \left(\frac{2\pi a^2 h\left(\frac{Y}{\sqrt{3}}\left(1 + \left[\frac{E}{\sqrt{3}Y}\right]^n \int_0^b \frac{(-\ln x)^n}{(1-x)}dx\right)\right)}{m}\right)^{\frac{1}{2}},$$
$$b = 1 - \frac{\sqrt{3}Y}{E}. \qquad \text{(Eq 4)}$$

Equation 4 reveals, in accordance with experimental findings, a weak nonlinear relationship between material strength (hardness) and the ballistic limit (V_{50}). While one should, in principle, use high-strain-rate material properties to compute V_{50} in Eq 4, it is generally found that the use of quasi-static material properties still yields reasonable predictions for V_{50} through Eq 4. This observation is generally rationalized using the fact that, under ballistic loading, material deformation is nearly adiabatic (i.e., heat conduction is practically absent), and hence, ductile hole-enlargement is controlled by the plastic deformation of the surrounding material at (practically) ambient temperature (at which high-strength steels typically show very little strain-rate sensitivity).

Plugging: Shear cracking is generally assumed to cause this mode of failure. Shear cracking is believed to be induced by the formation of adiabatic plastic-shear bands within the target-plate material surrounding the advancing blunt projectile (Ref 27, 29, 36). To model plugging-failure, the conservation equations and material constitutive relations are combined with
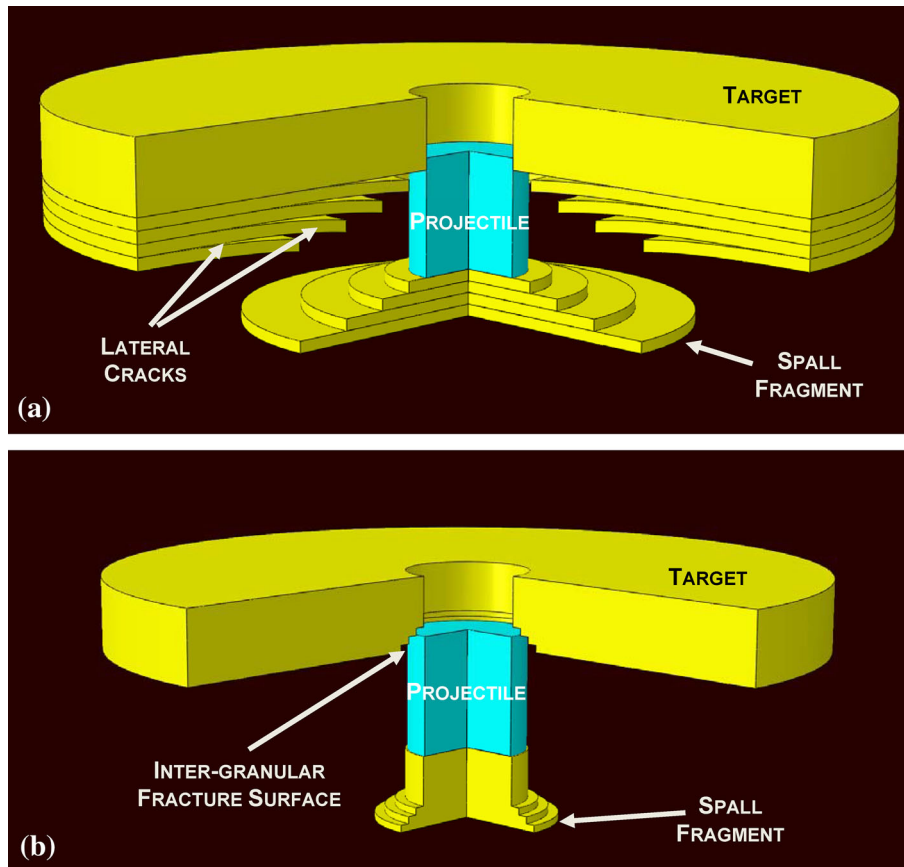
Fig. 14 Schematic representation of the spalling failure mechanism within the (a) HAZ; and (b) FZ regions

one of the adiabatic plastic-shear instability theories (e.g., Ref 36) in the present work.

Over the last 30 years, the phenomenon of adiabatic plastic-shear instability and its subsequent localization has been investigated extensively. Nowadays, it is believed that the essential physics behind adiabatic plastic-shear instability/localization is well understood. However, reliable quantitative relations between the onset of this failure mechanism and the material properties and loading conditions are required. The onset of plastic-shear strain instability is generally associated with a condition when, in the course of loading, strain-induced hardening becomes overmatched by the strain-induced softening processes. Under such conditions, the local rate of change of the maximum shear stress, τ, with the associated shear strain, γ, becomes non-positive, i.e.,

$$\frac{d\tau}{d\gamma} = \frac{\partial\tau}{\partial\gamma}\bigg|_{T,\dot{\gamma}} + \frac{\partial\tau}{\partial\dot{\gamma}}\bigg|_{T,\gamma}\frac{d\dot{\gamma}}{d\gamma} + \frac{\partial\tau}{\partial T}\bigg|_{\dot{\gamma},\gamma}\frac{dT}{d\gamma} \leq 0, \quad \text{(Eq 5)}$$

where a raised dot is used to denote a time derivative and T denotes temperature.

Under adiabatic conditions, the term $\frac{dT}{d\gamma}$ in Eq 5 can be set equal to τ/C, where C is the volumetric specific heat. As far as the remaining derivatives on the right-hand side of Eq 5 are concerned, their functional relationship depends on the $\tau(\gamma, \dot{\gamma}, T)$ relation used. For instance, if strain-hardening and strain-rate sensitivity relations are both assumed to be of a parabolic character with the corresponding exponents denoted, respectively, as n and m, Eq 5 can be re-written as:

$$\gamma_c = \frac{n}{\left(\frac{-1}{C}\frac{\partial\tau}{\partial T}\big|_{\gamma,\dot{\gamma}} - \frac{m}{\dot{\gamma}}\frac{d\dot{\gamma}}{d\gamma}\right)}, \quad \text{(Eq 6)}$$

where γ_c is a (minimum) critical value of the shear strain at the onset of plastic-shear strain instability at which $\frac{d\tau}{d\gamma} = 0$. In the high-strain-rate regime ($\dot{\gamma} > 100\,\text{s}^{-1}$) and for a typical range of values of the strain-rate sensitivity exponent ($0 < m < 1.0$), Eq 6 can be further simplified as:

$$\gamma_c = -\frac{Cn}{\left(\frac{\partial\tau}{\partial T}\big|_{\gamma,\dot{\gamma}}\right)} \quad \text{(Eq 7)}$$

Equation 7 reveals that the onset of plastic-shear strain instability and localization is delayed in materials in which:

(a) volumetric specific heat is relatively large and, hence, the associated adiabatic temperature increase is relatively small;

(b) strain-hardening effects are strong and can effectively counteract the effect of various softening processes; and

(c) temperature sensitivity of the material strength is not pronounced, so that local heating does not significantly reduce the material resistance toward plastic deformation.

Examination of Eq 6 and 7 reveals that they provide functional relationships between the critical shear strain at the onset of plastic-shear-strain localization and the material

constitutive response (properties). However, these equations do not explicitly address the target-material ballistic limit.

While it is well-established that plugging-failure is dominated by shear-strain localization, the task of establishing functional relationships between the associated ballistic limit and the material's propensity to plastic-shear-instability (as quantified by the critical shear strain, γ_c) is formidable. For example, while an increase in material hardness is generally found to increase the plugging-failure-controlled ballistic limit, this functional relationship is not reflected in Eq 6 and 7. Consequently, one would expect that high-hardness and high-strain-hardening target-materials would, in general, possess superior ballistic performance. However, in the case of welded joints, there is a trade-off between material hardness and its strain-hardening potential (i.e., these two material properties are inversely related and, hence, cannot be changed independently). Furthermore, it should be noted that the ballistic-limit scales with the energy absorbed by the target, which can be defined as an integral of stress over the associated strain path until localization. Consequently, at the lowest hardness levels and, thus, the highest strain-hardening levels, the onset of plastic-shear-strain instability is greatly delayed. However, the overall projectile kinetic energy absorption (i.e., the ballistic limit) remains low. As the target-material hardness increases, its ballistic limit increases due to the accompanying higher ability for energy absorption. In other words, the effect of an increase in the material strength/hardness more than compensates for the accompanying reduction in γ_c (caused by the associated reduction in the strain-hardening potential). At the highest hardness levels and, thus, the lowest strain-hardening levels, the target-material's ability to absorb projectile energy decreases due to the fact that the material becomes highly prone to plastic strain localization (a very small value of γ_c).

The aforementioned analysis reveals a complicated interplay between material hardness/strength, its strain-hardening behavior and its plugging-failure-controlled ballistic limit. This appears to be the main reason for the lack of a broadly accepted functional relationship between the plugging-failure-controlled ballistic limit and the target-material constitutive response/properties. To overcome this problem, a simple phenomenological model for the plugging-failure-controlled ballistic limit is developed in the remainder of this section. The model is based on the following simplifying assumptions/approximations:

(a) the projectile (of a right-circular cylindrical shape) remains undeformed during impact; and

(b) the kinetic energy of the projectile at the onset of plugging is exactly balanced by the work of plastic deformation in the shear-localization region surrounding the projectile as:

$$\frac{1}{2}\rho_{\mathrm{Proj}}\pi R_{\mathrm{Proj}}^2 h_{\mathrm{Proj}} V_{50}^2 = 2\pi R_{\mathrm{Proj}} h_{\mathrm{Target}}\delta R_{\mathrm{Shear}}\int_0^{\gamma_c}\tau d\gamma, \qquad \text{(Eq 8)}$$

where ρ denotes density, R the radius, h the thickness/height, δR the radial thickness and subscripts "Proj", "Target," and "Shear" represent the appropriate quantity in the projectile, target, and the plastic-shear-localization zone.

It should be noted that the present model contains only one adjustable parameter, $\delta R_{\mathrm{Shear}}$. This parameter has been determined by curve-fitting the plugging-failure-controlled ballistic-

limit experimental data for MIL A46100. Specifically, V_{50} versus h_{Target} data are taken from Ref 4. The data used pertain to the case of a 20 mm caliber, 53 g, blunt, chamfered right-circular cylindrical steel fragment simulating projectile or FSP (described, in greater detail, in the later portion of this section). Thus, all the quantities with subscript Proj appearing in Eq 8 are known. Then, for each pair of values of V_{50} and h_{Target}, $\delta R_{\mathrm{Shear}}$ is determined from Eq 8. Finally, an average value of $\delta R_{\mathrm{Shear}} = 0.4$ mm is obtained.

Spalling: This mode of failure possesses the following main characteristics: (a) typically occurs at the target back face; (b) is associated with a loss of the material through-the-thickness toughness; (c) usually gives rise to a substantial increase in the size of the projectile-exit hole (in the case of target defeat); and (d) gives rise to a loss in the target-material ballistic limit (particularly in the weld region characterized by large hardness and, thus, low toughness levels).

Although, over the last 30 years, spall failure has been investigated extensively, many aspects of this important phenomenon remain unresolved (e.g., Ref 37). This is the main reason that presently, there is no broadly accepted functional relation for the spall-failure-dominated ballistic limit. In the present work, no attempt will be made to derive this functional relationship. This decision was based on the following reasons:

(a) The overall contribution of the spalling failure to the ballistic limit of metallic welds is relatively small in comparison to the contributions associated with the ductile hole-enlargement and plugging-failure mechanisms; and

(b) Modeling of the spalling-controlled ballistic limit requires knowledge of the spatial distribution of material fracture toughness throughout the weld. However, the microstructure/property relationship module, even after the inclusions of the upgrades developed in the present work, is unable to provide predictions regarding the spatial distribution of fracture toughness within the weld.

3.2.3 Typical Results. The discussion in the previous subsection clearly established that the geometry of the projectile affects whether the ballistic limit of the target is controlled by hole-enlargement failure or plugging-failure. For this reason, separate predictions regarding the spatial distribution of V_{50} within the MIL A46100 GMAW joint are made for these two modes of target penetration.

Ductile hole-enlargement failure mode: In this case, the V_{50} velocity is calculated using Eq 4 (along with the local values for the material Young's modulus, yield strength, and exponent of strain-hardening). Only one type of projectile, a 7.62 mm caliber, 8.2 g, ogival-nose, steel-jacketed, hard tungsten core (1400 HV), and armor piercing (AP) projectile, was used in the analysis. The Young's modulus of the target is treated as a microstructure-insensitive property and, hence, assigned a constant value throughout the weld. The results displayed in Fig. 9(a) are used to assign the spatial distribution of the target-material yield strength/hardness within the joint. The local value of the exponents of strain-hardening throughout the weld was obtained by combining the results displayed in Fig. 9(a) with the functional relationship depicted in Fig. 10.

The spatial distribution of V_{50} yielded by this procedure is displayed in Fig. 15(a). The results displayed in this figure were obtained for the case of a 12.7 mm thick MIL A46100 armor-plate, welded under the same GMAW process and
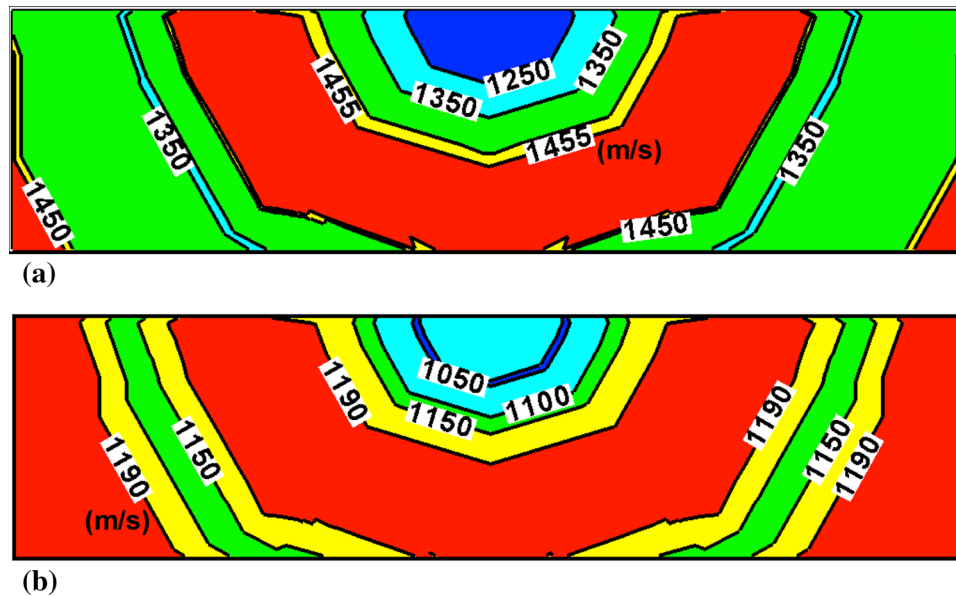
Fig. 15 Typical spatial distributions of the V_{50} (m/s) for the case of (a) ductile hole-enlargement failure; and (b) plugging-failure-controlled target penetration/ballistic-limit

base-/filler-metal conditions as the results presented in Fig. 8(a)-(f). Examination of Fig. 15(a) reveals that:

(a) there is a region within the FZ within which the ballistic limit has been reduced (by ca. 15%) below the level observed in the base-metal ca. 1455 m/s;

(b) there is a "critical region" within the HAZ within which V_{50} has dropped by 7-8% relative to its base-metal level. The presence of such critical regions within the HAZ has been reported in Ref 24; and

(c) in the particular case investigated here, the region associated with a lowered value of V_{50} represents a major portion ($>10\%$) of the weld. Therefore, one can expect that the presence of the GMAW joint will, in the case of direct impact, compromise the ballistic performance of the armor-plate.

Plugging-failure mode: In this case, the V_{50} velocity is calculated using Eq 7 and 8 (along with the local values of the volume-based heat capacity, material yield strength, exponent of strain-hardening, and the material shear-strength temperature-dependence $\frac{\partial \tau}{\partial T}\big|_{\gamma,\dot{\gamma}}$). A single projectile case, a 20 mm caliber, 53 g, blunt, and chamfered right-circular cylindrical steel FSP, is used in the analysis. As mentioned earlier, the volume-based heat capacity of the target is treated as a microstructure-insensitive property and assigned a constant value throughout the weld. The spatial distribution of the target-material yield strength within the joint is again taken from Fig. 9(a) and the exponent of strain-hardening is obtained by combining the results displayed in Fig. 9(a) with the functional relationship depicted in Fig. 10. As far as the temperature sensitivity of the material strength is concerned, it is assumed, as mentioned earlier, to have constant but different values within the FZ and HAZ (Ref 38-41).

The procedure described above yielded the spatial distribution of V_{50} as shown in Fig. 15(b). These results were obtained for the case of a 12.7 mm thick MIL A46100 armor-plate,

welded under the same GMAW process and base-/filler-metal conditions as the results presented in Fig. 8(a)-(f). Examination of the results displayed in Fig. 15(b), and their comparison with the results displayed in Fig. 15(a), reveals that:

(a) the overall spatial distribution of the ballistic limits with respect to the plastic-shear-localization and ductile hole-enlargement failure mechanisms are fairly similar; and

(b) the V_{50} values pertaining to the plastic-shear localization failure mode are consistently lower than their ductile hole-enlargement failure counterparts. This finding is fully consistent with the earlier discussion which indicated that, at high-strength levels, steels become more susceptible to shear-localization-induced failure under ballistic-impact conditions.

4. Summary and Conclusions

Based on the work presented and discussed in the present manuscript, the following main summary remarks and conclusions can be made:

(1) The five-module multi-physics computational model for the conventional GMAW joining process, developed in our recent work, has been expanded to include a sixth module. Within this module, the model is imparted the capabilities for predicting the spatial distribution of the mechanical properties controlling the ballistic limit (i.e., penetration-resistance) of the weld.

(2) The new module enables prediction of the all-metal welded-armor ballistic-limit under the condition that this limit is controlled by either ductile hole-enlargement or plugging-failure mechanisms.

(3) To demonstrate the utility of the upgraded GMAW process model, the case of a prototypical low-alloy,

high-hardness armor-grade martensitic steel, MIL A46100, welded-armor (with the filler-metal used being also MIL A46100) is analyzed.

(4) The work presented in this manuscript clearly revealed the capacity of the multi-physics GMAW process model to establish functional relationships between: (a) the process parameters, e.g., input welding voltage, electrode-to-workpiece distance, filler-metal feed-rate, welding-gun speed, etc.; (b) the resulting spatial distribution of the material microstructure (as represented by the volume fractions of various crystallographic phases and micro-constituents as well as by the prior-austenite grain size); (c) the associated mechanical properties (e.g., strength/hardness, stiffness, exponent of strain-hardening, etc.); and (d) the ballistic-limit/penetration-resistance within the fusion and the heat-affected zones of the weld.

Acknowledgments

References

1. M. Grujicic, S. Ramaswami, J.S. Snipes, C.-F. Yen, B.A. Cheeseman, and J.S. Montgomery, Multi-physics Modeling and Simulations of MIL A46100 Armor-Grade Martensitic Steel Gas Metal Arc Welding Process, *J. Mater. Eng. Perform.*, 2013, **22**, p 2950–2969

2. M. Grujicic, S. Ramaswami, J.S. Snipes, R. Yavari, A. Arakere, C.-F. Yen, and B.A. Cheeseman, Computational Modeling of Microstructure Evolution in AISI, 1005 Steel During Gas Metal Arc Butt Welding, *J. Mater. Eng. Perform.*, 2012, **22**, p 1209–1222

3. M. Grujicic, A. Arakere, S. Ramaswami, J.S. Snipes, R. Yavari, C.F. Yen, B.A. Cheeseman, and J.S. Montgomery, Gas Metal Arc Welding Process Modeling and Prediction of Weld Microstructure in MIL A46100 Armor-Grade Martensitic Steel, *J. Mater. Eng. Perform.*, 2013, **22**, p 1541–1557

4. M.G.H. Wells, R.K. Weiss, and J.S. Montgomery, *"LAV Armor Plate Study", MTL TR 92-26*, U.S. Army Materials Technology Laboratory, Watertown, MA, 1992

5. M. Grujicic, G. Arakere, B. Pandurangan, A. Hariharan, C.F. Yen, B.A. Cheeseman, and C. Fountzoulas, Computational Analysis and Experimental Validation of the Ti-6Al-4V Friction Stir Welding Behavior, *J. Eng. Manuf.*, 2010, **224**, p 1–16

6. M. Grujicic, T. He, G. Arakere, H.V. Yalavarthy, C.F. Yen, and B.A. Cheeseman, Fully-Coupled Thermo-mechanical Finite-Element Investigation of Material Evolution During Friction-Stir Welding of AA5083, *J. Eng. Manuf.*, 2010, **224**, p 609–625

7. M. Grujicic, G. Arakere, H.V. Yalavarthy, T. He, C.F. Yen, and B.A. Cheeseman, Modeling of AA5083 Material-Microstructure Evolution During Butt Friction-Stir Welding, *J. Mater. Eng. Perform.*, 2010, **19**, p 672–684

8. M. Grujicic, G. Arakere, B. Pandurangan, A. Hariharan, C.F. Yen, and B.A. Cheeseman, Development of a Robust and Cost-Effective Friction Stir Welding Process for Use in Advanced Military Vehicle Structures, *J. Mater. Eng. Perform.*, 2011, **20**, p 11–23

9. M. Grujicic, G. Arakere, C.F. Yen, and B.A. Cheeseman, Computational Investigation of Hardness Evolution During Friction-Stir Welding of AA5083 and AA2139 Aluminum Alloys, *J. Mater. Eng. Perform.*, 2011, **20**, p 1097–1108

10. M. Grujicic, G. Arakere, A. Hariharan, and B. Pandurangan, A Concurrent Product-Development Approach for Friction-Stir Welded Vehicle-Underbody Structures, *J. Mater. Eng. Perform.*, 2012, **21**, p 437–449

11. M. Grujicic, G. Arakere, A. Hariharan, and B. Pandurangan, Two-Level Weld-Material Homogenization Approach for Efficient Computational Analysis of Welded Structure Blast Survivability, *J. Mater. Eng. Perform.*, 2012, **21**, p 786–796

12. M. Grujicic, G. Arakere, B. Pandurangan, J.M. Ochterbeck, C.F. Yen, B.A. Cheeseman, A.P. Reynolds, and M.A. Sutton, Computational Analysis of Material Flow During Friction Stir Welding of AA5059 Aluminum Alloys, *J. Mater. Eng. Perform.*, 2012, **21**, p 1824–1840

13. M. Grujicic, B. Pandurangan, C.-F. Yen, and B.A. Cheeseman, Modifications in the AA5083 Johnson-Cook Material Model for Use in Friction Stir Welding Computational Analyses, *J. Mater. Eng. Perform.*, 2012, **21**, p 2207–2217

14. M. Gore, M. Grujicic, and G.B. Olson, Thermally Activated Grain Boundary Motion Through a Dispersion of Particles, *Acta Metall.*, 1989, **37**, p 2849–2854

15. W.S. Owen and M. Grujicic, *Encyclopedia of Materials Science and Engineering, Section—"Plastic Deformation: Thermally Activated Glide of Dislocations"*, Pergamon Press, Oxford, UK, 1986, p 3540–3543

16. R.L. Fleischer, Substitutional Solution Hardening, *Acta Metall. Mater.*, 1963, **11**, p 203–209

17. R. Labusch, A Statistical Theory of Solid Solution Hardening, *Phys. Status Solidi*, 1970, **41**, p 659–669

18. M.F. Ashby, *On the Orowan Stress*, M.F. Ashby, Ed., The M.I.T. Press, Cambridge, MA, 1969, p 113–131

19. M. Takahashi and H.K.D.H. Bhadeshia, Model for Transition from Upper Bainite to Lower Bainite, *Mater. Sci. Technol.*, 1990, **6**, p 592–603

20. A.S. Keh and S. Weissman, *Deformation Structure in Body-Centered Cubic Metals*, A.S. Keh and S. Weissman, Ed., Interscience, New York, 1963, p 231–300

21. W.C. Leslie, J.T. Michalak, and F.W. Aul, *The Annealing of Cold-Worked Iron*, W.C. Leslie, J.T. Michalak, and F.W. Aul, Ed., Interscience, Detroit, 1961, p 119–212

22. R.E. Reed-Hill and R. Abbaschian, *Physical Metallurgy Principles*, 3rd ed., PWS-Kent Publishing Co., Boston, MA, 1992

23. M.F. Ashby and D.R.H. Jones, *Engineering Materials: An Introduction to Their Properties and Application*, Pergamon Press, New York, 1980

24. J.S. Unfried, C.M. Garzón, and J.E. Giraldo, Numerical and Experimental Analysis of Microstructure Evolution During Arc Welding in Armor Plate Steels, *J. Mater. Process. Technol.*, 2009, **209**, p 1688–1700

25. Cambridge Engineering Selector, http://www.grantadesign.com/. Accessed December 31, 2013

26. A.M. Sarosiek, M. Grujicic, and W.S. Owen, The Importance of the Heterogeneity of the Deformation in the Ferrite Phase of a Dual-Phase Steel, *Scripta Metall.*, 1984, **8**, p 353–356

27. G.G. Corbett, S.R. Reid, and W. Johnson, Impact Loading of Plates and Shells by Free-Flying Projectiles: A Review, *Int. J. Impact Eng.*, 1996, **18**, p 141–230

28. K.S. Kumar, D. Singh, and T. Bhat, Studies on Aluminum Armour Plates Impacted by Deformable and Non-deformable Projectiles, *Mater. Sci. Forum*, 2004, **465–466**, p 79–84

29. T. Børvik, O.S. Hopperstad, and K.O. Pedersen, Fracture Mechanisms of Aluminum Alloy AA7075-T651 Under Various Loading Conditions, *Int. J. Impact Eng.*, 2010, **37**, p 537–551

30. T. Børvik, M.J. Forrestal, O.S. Hopperstad, T.L. Warren, and M. Langseth, Perforation of AA5083-H116 Aluminium Plates with Conical-Nose Steel Projectiles—Calculations, *Int. J. Impact Eng.*, 2009, **36**, p 426–437

31. M.R. Edwards and A. Mathewson, The Ballistic Properties of Tool Steel as a Potential Improvised Armor Plate, *Int. J. Impact Eng.*, 1997, **19**, p 297–309

32. M.J. Forrestal, V.K. Luk, and N.S. Brar, Penetration of Aluminum Armor Plates with Conical-Nose Projectiles, *Mechanics*, 1990, **10**, p 97–105

33. A.J. Piekutowski, M.J. Forrestal, K.L. Poormon, and T.L. Warren, Ogive-Nose Steel Rods at Normal, *Int. J. Impact Eng.*, 1996, **18**, p 877–887

34. T. Børvik, A.H. Clausen, O.S. Hopperstad, and M. Langseth, Perforation of AA5083-H116 Aluminium Plates with Conical-Nose Steel Projectiles—Experimental Study, *Int. J. Impact Eng.*, 2004, **30**, p 367–384

35. A.H. Chausen, T. Børvik, O.S. Hopperstad, and A. Benallal, Tore Flow and Fracture Characteristics of Aluminium Alloy AA5083-H116 as Function of Strain Rate, Temperature and Triaxiality, *Mater. Sci. Eng.*, 2004, **A364**, p 260–272

36. T. Børvik, J.R. Leinum, J.K. Solberg, O.S. Hopperstad, and M. Langseth, Observations on Shear Plug Formation in Weldox 460 E Steel Plates Impacted by Blunt-Nosed Projectiles, *Int. J. Impact Eng.*, 2001, **25**, p 553–572

37. A.P. Rybakov, Spall in Non-one-dimensional Shock Waves, *Int. J. Impact Eng.*, 2000, **24**, p 1041–1082

38. M. Grujicic, G.B. Olson, and W.S. Owen, Kinetics of Martensitic Interface Motion, Proc. ICOMAT-82, Leuven, Belgium, *J. Physique*, 1982, **43**(Suppl. 12), pp. C4-173–179

39. M. Grujicic and G. Haidemenopoulos, Treatment of Paraequilibrium Thermodynamics in an AF1410 Steel Using the Thermo-Calc Software and Database, *Calphad*, 1988, **12**(3), pp. 219–224

40. M. Grujicic, I.J. Wang, and W.S. Owen, On the Formation of Duplex Precipitate Phases in an Ultra-low Carbon Micro-alloyed Steel, *Calphad*, 1988, **12**(3), pp. 261–275

41. M. Grujicic, G. Cao, and G.M. Fadel, "Effective Materials Properties: Determination and Application in Mechanical Design and Optimization," *J. Mater.: Des. Appl.*, 2002, **215**, pp. 225–234